CONDENSED MATTER PHYSICS

Imaging mesoscopic antiferromagnetic spin textures in the dilute limit from single-geometry resonant coherent x-ray diffraction

Martin Bluschke[1]*†‡, Rourav Basak[2]‡, Andi Barbour[3], Ashley N. Warner[2]†, Katrin Fürsich[1], Stuart Wilkins[3], Sujoy Roy[4], James Lee[4,5], Georg Christiani[1], Gennady Logvenov[1], Matteo Minola[1], Bernhard Keimer[1], Claudio Mazzoli[3], Eva Benckiser[1], Alex Frano[2]*

The detection and manipulation of antiferromagnetic domains and topological antiferromagnetic textures are of central interest to solid-state physics. A fundamental step is identifying tools to probe the mesoscopic texture of an antiferromagnetic order parameter. In this work, we demonstrate that Bragg coherent diffractive imaging can be extended to study the mesoscopic texture of an antiferromagnetic order parameter using resonant magnetic x-ray scattering. We study the onset of the antiferromagnet transition in $PrNiO_3$, focusing on a temperature regime in which the antiferromagnetic domains are dilute in the beam spot and the coherent diffraction pattern modulating the antiferromagnetic peak is greatly simplified. We demonstrate that it is possible to extract the arrangements and sizes of these domains from single diffraction patterns and show that the approach could be extended to a time-structured light source to study the motion of dilute domains or the motion of topological defects in an antiferromagnetic spin texture.

INTRODUCTION

Over the past decades, a variety of experimental techniques have emerged, making it possible to image antiferromagnetic textures over mesoscopic length scales. While some of these techniques probe antiferromagnetism directly, for example, by accessing an antiferromagnetic Bragg condition in a diffraction experiment, the wide majority probe antiferromagnetism indirectly, such as optical birefringence (*1*, *2*), or linear dichroic x-ray microscopies (*3*, *4*), which are sensitive to the spin-orbit coupling–mediated effect of antiferromagnetism on the surrounding electronic and structural environment. The need for a direct probe of antiferromagnetism becomes particularly acute in materials with technologically relevant couplings between lattice, spin, charge, and orbital degrees of freedom. For example, the rare-earth nickelates $PrNiO_3$ and $NdNiO_3$ exhibit a propensity toward a correlation-driven insulating ground state, characterized by a bond order and a coupled noncollinear antiferromagnetic order with twice the periodicity. In $NdNiO_3$, both linear dichroic x-ray photoemission electron microscopy and scanning near-field optical microscopy (SNOM) have been successful in imaging the metal-insulator transition (*5*, *6*) but are less sensitive to the noncollinear antiferromagnetism of the Ni spins. While certain anomalous features in the nano-infrared response probed by SNOM were interpreted as arising from the presence of antiferromagnetic antiphase domain boundaries, the first direct identification of the antiferromagnetic domain morphology in this material was reported using resonant magnetic Bragg scattering applied in a scanning mode (*7*).

Antiferromagnetic imaging techniques can be further broken down into scanning-type and single-shot (single-geometry) experiments. Scanning techniques to study antiferromagnetism are the most common and have been implemented for both direct and indirect probes. These include both resonant and nonresonant scanning magnetic diffraction (*7*, *8*), spin-polarized scanning tunneling microscopy (*9*), magneto-optical Kerr effect microscopy, magnetic force microscopy (*10*), spatially resolved second harmonic generation (*11*), magnetic linear dichroic scanning transmission x-ray microscopy (STXM) (*12*), and others (*13*–*15*). While scanning techniques are numerous and produce relatively simple-to-interpret images, they are inherently slow and therefore often cannot be extended to capture dynamically evolving systems. Some notable exceptions exist, for example, stroboscopic time-resolved STXM (*16*) and stroboscopic resonant magnetic dichroic ptychography (*17*), which have been used to capture spatially resolved magnetization dynamics.

To image the dynamics and collective excitations associated with antiferromagnetic textures, it would be desirable to identify a nonscanning imaging modality with direct sensitivity to antiferromagnetism. Recently, resonant x-ray Bragg diffraction phase contrast microscopy (XBPM) (*18*) was used to resolve images of antiphase domain boundaries, directly visible on the tails of the specular (001) magnetic Bragg reflection in the collinear antiferromagnet $Fe_2Mo_3O_8$. This result represents an important step forward for coherent x-ray–based imaging of antiferromagnetic domain structures, although it remains to be seen with what generality XBPM can be applied. Here, we continue on a related path by demonstrating that a special case of the Bragg coherent diffractive imaging (BCDI) (*19*) technique can be applied to study the mesoscopic features of a two-dimensional antiferromagnetic texture, using resonant x-rays to achieve sensitivity to antiferromagnetic Bragg scattering. From a single-shot geometry, we extract a two-dimensional image of the

[1]Max Planck Institute for Solid State Research, Heisenbergstr. 1, 70569 Stuttgart, Germany. [2]Department of Physics, University of California San Diego, La Jolla, CA 92093, USA. [3]NSLS-II, Brookhaven National Laboratory, Upton, NY 11973, USA. [4]Advanced Light Source, Lawrence Berkeley National Laboratory, Berkeley, CA 94720, USA. [5]Department of Physics, Concordia College, Moorhead, MN 56562, USA.
*Corresponding author. Email: martin.bluschke@ubc.ca (M.B.); afrano@ucsd.edu (A.F.)
†Present address: Quantum Matter Institute, University of British Columbia, Vancouver, BC, V6T 1Z4, Canada.
‡These authors contributed equally to this work.

sizes and relative positions of the first domains formed in the antiferromagnetic transition of a [001]-oriented $PrNiO_3$ thin film. The particular success of our approach hinges on the dilute character of the domain configurations in the nucleation regime, as well as the inherent two-dimensionality imposed by the thin film geometry. The dilute finite-sized domains provide a natural support (finite extent of the probed object) and simultaneously ensure oversampling of the coherent speckle pattern in the far field. Provided that the necessary sampling requirements (*20*) are fulfilled, the BCDI modality we demonstrate should be extendable not only to domain and domain wall imaging in other antiferromagnets but also to the imaging of topological defects in antiferromagnetic spin textures. In a broader context, the combination of resonant x-ray scattering and BCDI may be extended to a wider range of domain structure types associated with charge and orbital orders, whose x-ray scattering cross sections can also be strongly enhanced on resonance.

RESULTS

The correlated antiferromagnetic ground state observed in the rare-earth nickelates is of interest both fundamentally and for technological application. In the past years, the noncollinear antiferromagnetism observed in $LaNiO_3$, $PrNiO_3$, and $NdNiO_3$ has been studied extensively both in thin films (*6*, *7*, *21*–*23*) and in multilayer heterostructures (*24*–*27*). Here, we investigate the antiferromagnetic transition in a 40-nm $PrNiO_3$ thin film using coherent x-rays tuned to the $2p \rightarrow 3d$ electronic transition of the Ni ions. This electronic resonance is referred to as the Ni L_3 resonance, and it can be exploited to embed valuable information in the x-ray scattering cross section about the valence $3d$ electronic states and, for example, the antiferromagnetism that they host. Transverse and longitudinal x-ray beam coherence lengths on the order of micrometers enable sensitivity to mesoscopic real-space structures with comparable length scales. Figure 1A shows a schematic of the resonant coherent x-ray diffraction (RCXD) experimental setup. The orientation of the sample and the position of the detector are chosen with respect to the incidence beam such that the antiferromagnetic Bragg peak at momentum transfer $\mathbf{q}_{\mathrm{AFM}} = \left(\frac{1}{4}\frac{1}{4}\frac{1}{4}\right)_{\mathrm{pc}}$ is recorded on the detector. The temperature dependence of this diffraction intensity is plotted in Fig. 1B and compared with the DC electrical resistance of the film. As expected in this system, both signals are hysteretic, indicative of the first-order nature of this phase transition.

The unexpected feature of our data is observed for temperatures near the critical temperature of the antiferromagnet (highlighted in Fig. 1B). In this temperature regime, the antiferromagnetic diffraction peak is modulated by a small-**q** superstructure. This is in contrast to the typical speckle pattern (*28*) that is observed at lower temperatures, where the insulating antiferromagnetic phase is well established. In Fig. 1B, examples of the magnetic Bragg peak at various temperatures are used to demonstrate the evolution of the diffraction pattern through one full cooling and warming cycle.

Because of the coherence of the x-ray beam, interference between x-rays scattered at mesoscopic distances from one another (up to micrometers) is capable of producing a modulation of the Bragg peak intensity in reciprocal space. These modulations encode information about the relative sizes, positions, shapes, and phases of the domains from which the x-rays are scattered. In the limit of many domains distributed across the entire beam spot, the resulting modulations are complex, and the speckle size is inversely related to the size of the beam (*29*). Such a typical speckle pattern is observed on the low-temperature antiferromagnetic Bragg peak in Fig. 1B. However, in the limit of very few scatterers occupying only a portion of the beam spot, well-defined oscillations of the Bragg peak intensity are observed in reciprocal space and can be directly interpreted in terms of the real-space distances between domains or domain boundaries. This is the same regime that gives rise to the small-**q** modulations associated with the finite size of a nanocrystal in a nonresonant BCDI experiment, e.g., the fringes on the (111) Bragg peak of a gold nanocrystal reported by Robinson *et al.* (*19*). Related effects have also been demonstrated in nonresonant BCDI from a periodic array of GeSi nanostructures (*30*). In contrast to these examples, in which mesoscopic structural features were investigated, our study represents the first observation of a small-**q** modulation of an antiferromagnetic Bragg peak associated with the mesoscopic domain arrangement of the antiferromagnetic order. In our experiment, the small-**q** superstructure observed near the critical temperature is interpreted in terms of interference between the very first few domains to undergo the antiferromagnetic transition. The appearance of bubbles of antiferromagnetically ordered spins on the background of a disorderd spin lattice is consistent with the bulk bimodal nature of the metal-insulator transition observed in the closely related material $NdNiO_3$ (*6*).

In an RCXD experiment, although the phase of the incident light is well defined, the phases of the scattered x-rays are lost at the detector, where the collected intensities correspond to the absolute value squared of the spatial Fourier transform of the electronic states selected in the resonant process. This is known as the so-called phase problem, which implies that the real-space arrangement of the scatterers cannot be directly retrieved by applying an inverse Fourier transform to the recorded diffraction pattern without some additional information about the phase of the scattered x-rays (or preexisting information about the real-space arrangement of the scatterers). The phase problem can be overcome using either holography approaches, which make use of a reference beam with known phase to determine the phase of the scattered light (*31*), or ptychographic (*32*) and coherent diffractive imaging methods (*33*), which are based on iterative reconstruction algorithms (*34*, *35*). For the purpose of our proof of principle, we focus explicitly on the limit of very few scatterers, which we will refer to as the "dilute" coherent scattering regime. Working in the dilute regime, the small-**q** modulations of the antiferromagnetic Bragg peak can be interpreted by eye and modeled by trial and error based on knowledge of the system. Because of the heightened likelihood of a unique solution to the phase problem in two dimensions (*36*, *37*), one can be reasonably confident that the model that reproduces the observed diffraction pattern is correct, thereby circumventing the need for a complex phase retrieval algorithm.

To model the small-**q** modulations of the antiferromagnetic Bragg peak, we take the absolute value squared of the Fourier transform of small numbers of staggered antiferromagnetic domains, whose spatial arrangement is chosen to reflect the symmetries of the modulation patterns. By translating the beam across the sample, we were able to identify the observed coherent diffraction patterns as location specific, disappearing when the beam is translated by approximately one beam width. On the basis of this observation, we exclude repeating structures with the same symmetry as the determined domain arrangements. A domain configuration with the minimum number of domains needed to reproduce the observed modulation

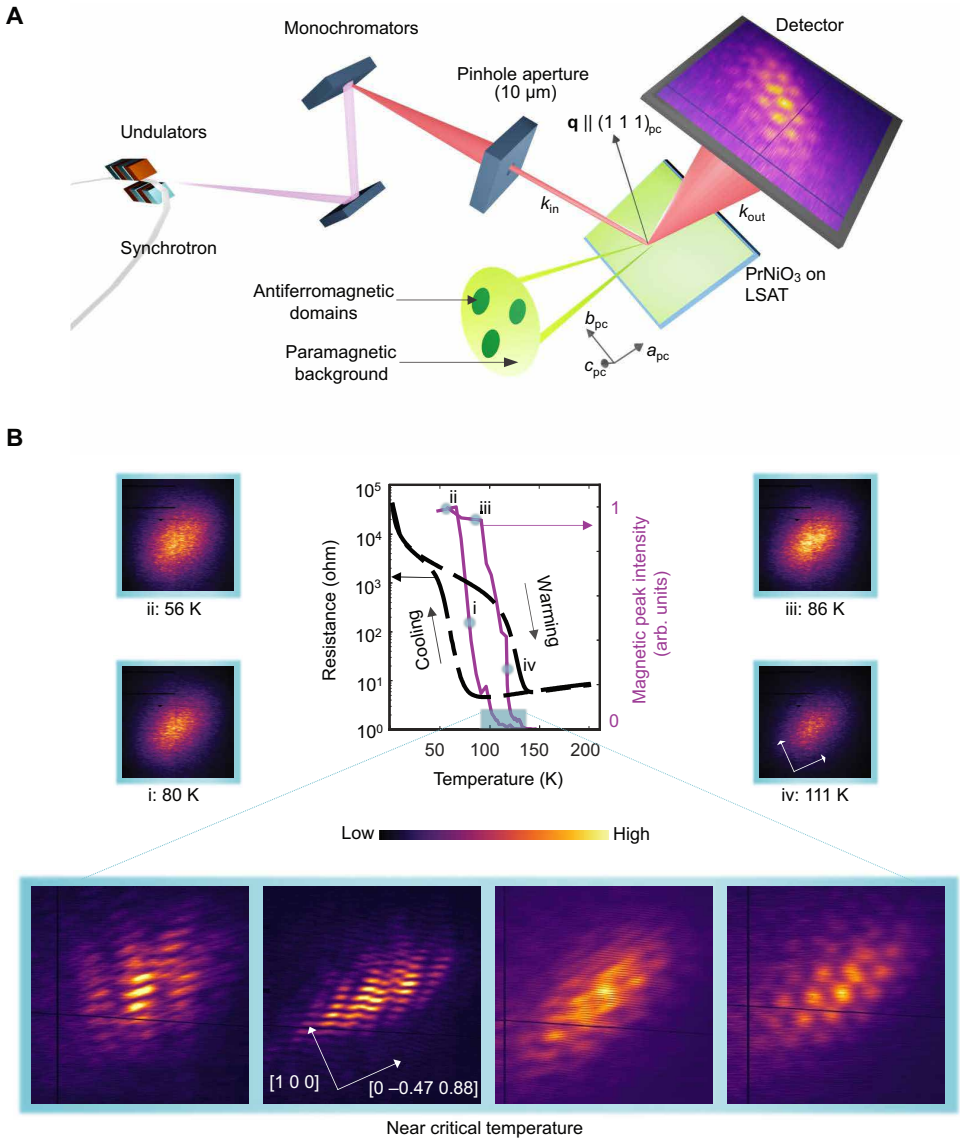

Fig. 1. Experimental setup and thermal evolution of antiferromagnetic RCXD patterns. (**A**) Experimental setup, where a partially coherent beam of synchrotron radiation is produced by an elliptical undulator and monochromated. Immediately before reaching the sample, the beam passes through a 10-μm pinhole. The scattering geometry probes the pseudocubic $\left(\frac{1}{4}\frac{1}{4}\frac{1}{4}\right)_{pc}$ reciprocal space position, corresponding to the first-order antiferromagnetic Bragg peak of the Ni spin spiral in the perovskite nickelate $PrNiO_3$. (**B**) Data from a $PrNiO_3$ thin film. The central plot compares the normalized temperature-dependent antiferromagnetic scattering intensity with the van der Pauw resistance measured ex situ on the same film. The surrounding charge-coupled device images demonstrate the evolution of the antiferromagnetic Bragg peak as a function of temperature across the first-order antiferromagnetic/metal-insulator transition. The white arrows are shown once for the small-format images and once for the large-format images and can be interpreted as scale bars with a magnitude of 0.001 $Å^{-1}$. The directions indicated correspond to (1 0 0) (momentum transfer parallel to the sample surface) and (0 – 0.47 0.88), which has the largest projection onto (0 0 1) (momentum transfer in the film growth direction). In the temperature region near the critical temperature, pronounced small-**q** modulations are observed on top of the magnetic Bragg peak. The scale of each color bar has been chosen individually to maximize the visibility of the speckle and small-**q** modulation patterns. The total (integrated) intensity of each peak is indicated with a light blue circle in the central plot.

pattern is consistent with the approximate space filling of the ordered phase, which is small at the onset of the transition. Guiding the modeling process in this way quickly produces a simple real-space image of the relative positions and sizes of the first antiferromagnetic domains formed in the illuminated region of the film. Note that this level of analysis does not capture the detailed shape of the domains, which are given an ellipsoidal profile to reproduce the observed peak elongation (see Materials and Methods). In general, any first-order phase transition with some degree of spatial inhomogeneity is expected to exhibit a dilute set of nucleation sites in some temperature regime near the ordering temperature. In the current system, cycling of the temperature through the phase transition reveals that the first antiferromagnetic domains formed in the nucleation regime reappear at the same locations (see the Supplementary Materials), thereby indicating that the seeding centers are likely pinned to structural features that are immobile for temperatures up

to the maximum cycling temperature of 300 K. The substrate may play an important role in determining this spatial inhomogeneity, for example, via inhomogeneous strain fields, structural domain patterns, or step edges of the substrate's terraced surface, all of which may locally suppress or seed the metal-insulator transition and accompanying antiferromagnetism.

The results of our modeling process are demonstrated for two diffraction patterns in Fig. 2. The Fourier transforms of the model domain configurations agree well with the measured diffraction patterns, even without the application of a numerical fitting algorithm to optimize the fits. The additional background intensity and reduced speckle contrast observed in the experimental data may arise in part from short-range antiferromagnetic fluctuations, which are not captured in our model. We emphasize that although the solution to the real-space domain arrangement remains ambiguous with respect to the trivial operation translation, phase shift, and inversion conjugation, the two-dimensional nature of the probed domain arrangement allows us to exclude more complex alternate solutions (*36*, *37*). While inversion of our coherent scattering data using an iterative phase retrieval algorithm was beyond the scope of this study, our results imply that the numerical inversion of such resonant coherent antiferromagnetic diffraction data is possible in the dilute limit and will likely be capable of both resolving finer domain morphology features and extracting information from the complex speckle diffraction patterns observed at low temperatures, provided that the necessary sampling conditions are observed (*20*).

In the following outlook section, we consider hypothetical dynamically driven magnetic textures and argue that time-resolved RCXD, in the dilute scattering limit, presents a powerful opportunity to study the motion of antiferromagnetic domains or topological defects in an antiferromagnetic spin texture. Figure 3 (A to E) depicts a series of hypothetical dilute antiferromagnetic domain configurations in real space. Figure 3A corresponds to a single circular domain, whereas Fig. 3 (B to D) depicts snapshots of one domain passing in between two other domains of equal size and then disappearing in Fig. 3E. The diffraction patterns in the vicinity of the first-order antiferromagnetic Bragg peak originating from each of the real-space domain arrangements shown in Fig. 3 (A to E) are simulated in Fig. 3 (F to J), respectively. The number and relative positions of the probed domains are clearly reflected in the symmetries of the small-**q** modulations of the antiferromagnetic Bragg peak intensity.

Next, we extend the concept of dilute magnetic textures to encompass the notion of a dilute set of topological defects on an antiferromagnetic lattice, such as antiferromagnetic knife edge dislocations observed in the skyrmion nucleation regime of helical antiferromagnets (*38*), or theoretically predicted antiferromagnetic vortices and skyrmions (*39*, *40*). Figure 3 (P to T) demonstrates the sensitivity of the simulated RCXD cross section around a first-order antiferromagnetic Bragg peak to the presence and relative arrangements of a dilute set of antiferromagnetic vortices depicted in real space in Fig. 3 (K to O). The diffraction patterns in Fig. 3 (P to T)

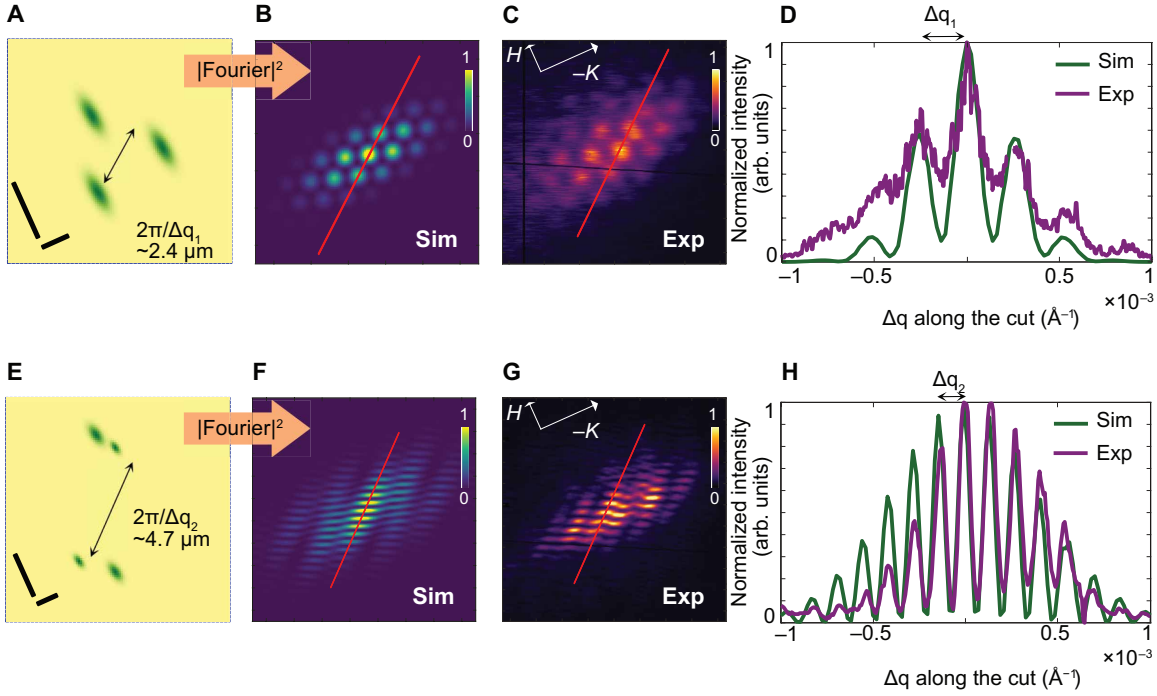

Fig. 2. Modeling of experimental RCXD patterns. (**A**) Model configuration in real space of three antiferromagnetic domains within the beam spot. The scale bars correspond to 2 μm along the [100] direction (long bar) and along the [010] direction (short bar). (**B**) Absolute value squared of the Fourier transform of the model shown in (A). Scale bars are the same as in (C). (**C**) Experimentally observed reciprocal space map of the antiferromagnetic Bragg peak at momentum transfer $\mathbf{q}_{AFM} = \left(\frac{1}{4}\frac{1}{4}\frac{1}{4}\right)_{pc}$ in the pseudocubic setting of $PrNiO_3$. After projecting the detector image onto the *H*-*K* plane, the lengths of the arrows labeled *H* and *K* correspond to 0.001 $Å^{s-1}$, respectively, along the (100) and (010) directions. (**D**) Comparison of cuts taken from (B) and (C) along the indicated red line. A constant has been subtracted from the experimental curves such that the intensity at the detector edge is zero. (**E** to **H**) Same as (A) to (D) but for a different experimentally observed diffraction pattern (G) and the corresponding model and simulation in (E) and (F).

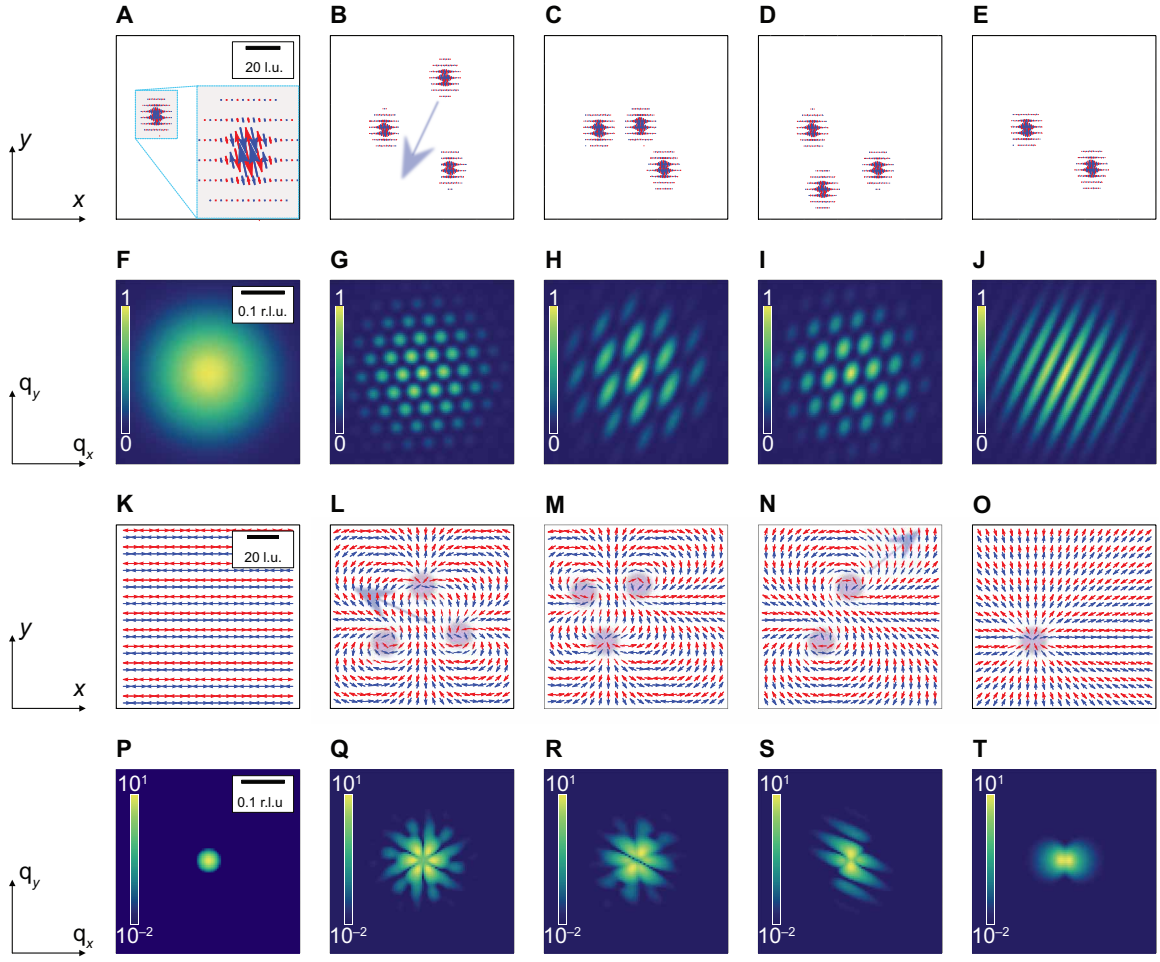

Fig. 3. Simulation of RCXD from mobile antiferromagnetic domain arrangements and antiferromagnetic topological spin textures. (**A**) Single antiferromagnetic domain in two dimensions. (**B** to **D**) Three equally sized antiferromagnetic domains, one moving with respect to the other stationary two. (**E**) Two equally sized antiferromagnetic domains. (**F** to **J**) Absolute value squared of the Fourier transforms of the model domain configurations in (A) to (E). (**K**) Uniform antiferromagnetism in two dimensions. (**L** to **O**) Antiferromagnetic vortices with topological winding number $w = 1$. The centers of the vortices are indicated by a shaded disc. (**P** to **T**) Absolute value squared of the Fourier transforms of the spin x component for the antiferromagnetic spin textures shown in (K) to (O). The number of angular nodes corresponds to twice the sum of the winding numbers of all vortices in the beam spot. Scale bars correspond to 20 lattice units (l.u.) and 0.1 reciprocal lattice units (r.l.u.) in the real and Fourier space images respectively.

correspond to a resonant magnetic scattering polarization channel that selects the spin x component. In Fig. 3 (K and P), the trivial case of a homogeneously ordered antiferromagnetic lattice is considered, whereas Fig. 3 (L, M, Q, and R) illustrates the motion of one antiferromagnetic vortex past two stationary vortices. Removing vortices from the beam spot, Fig. 3 (N and S) corresponds to just a pair of antiferromagnetic vortices, and Fig. 3 (O and T) corresponds to a single vortex. For the purposes of this demonstration, we considered equal antiferromagnetic vortices, each corresponding to a topological defect of winding number $w = 1$, with the spins winding in the plane of the lattice. Similar scattering signatures are expected to arise in the presence of antiferromagnetic skyrmions (*39*, *40*), where the antiferromagnetic spin orientations wind in three dimensions. Note that in our results, the number of angular nodes in the simulated antiferromagnetic Bragg intensity corresponds to twice the number of $w = 1$ vortices present in the beam spot or, more generally, the net topological charge of the spin texture contained within the beam spot. This indicates an important quantitative sensitivity of the RCXD cross section to the mesoscopic winding of the antiferromagnetic order parameter, reminiscent of the results of Zhang *et al.* (*41*) in the skyrmion material Cu_2OSeO_3, or the resonant x-ray scattering method for determining the topological invariant of nondegenerate band crossings in Weyl semimetals proposed by Kourtis (*42*).

DISCUSSION

Here, we have shown that the RCXD signal at an antiferromagnetic Bragg condition can be analyzed in the sense of a BCDI experiment to extract information about the mesoscopic texture of an antiferromagnetic order parameter. Furthermore, we have demonstrated the particular utility of working in the dilute scattering regime, which, when combined with a quasi–two-dimensional sample geometry, can facilitate the direct interpretation of single-shot RCXD diffraction patterns in terms of real-space domain arrangements. These results naturally raise the question as to which specific systems could benefit from this experimental approach. Of all first-order antiferromagnets, the described technique will be limited to those that have accessible antiferromagnetic reflections at the relevant

resonant photon energies. For example, magnetocaloric materials in the family $Gd_5(Si_xGe_{1-x})_4$ have been synthesized in thin-film form (*43*) and are known to exhibit a first-order antiferromagnetic-ferromagnetic transition as a function of temperature and magnetic field. The antiferromagnetism on the Gd sites can be probed by resonant magnetic x-ray scattering (*44*) and is known to coexist in a spatially separated manner with competing ferromagnetic domains in the vicinity of the transition (*45*). An equilibrium RCXD study of the Gd antiferromagnetism as the antiferromagnetic phase is approached with field or temperature may be capable of imaging this phase coexistence in the antiferromagnetic nucleation regime. If so, the dynamic melting and reforming of dilute domain configurations may be studied in a pump-probe experiment, using an optical excitation to transiently heat the electronic system above the Neel temperature. We expect that a similar pump-probe analysis of the domain melting and reforming will also be applicable to the first-order antiferromagnetic phase transition observed in the $PrNiO_3$ film studied here, as well as the related compound $NdNiO_3$.

Another candidate family of systems for RCXD studies are the magnetic honeycomb iridates, which exhibit strongly spin-anisotropic exchange interactions and may be capable of supporting a quantum spin liquid ground state. A recent resonant magnetic x-ray scattering study of β-Li_2IrO_3 demonstrated a field-induced crossover from an incommensurate antiferromagnetic state to a so-called field-induced zig-zag state (*46*) at 2.8 T. An equilibrium RCXD study in the onset region of the noncollinear antiferromagnetism will help to determine whether these competing magnetic states coexist locally or are spatially segregated in the crossover regime, a question that is currently under debate. Similarly, an RCXD investigation of the pressure-induced hidden order to large-moment antiferromagnetic transition in the heavy-fermion superconductor URu_2Si_2 would help to identify the possible existence and nature of phase coexistence below the critical pressure. Even at ambient pressure, dilute patches of antiferromagnetism within the hidden order phase may give rise to a small-**q** modulation of the antiferromagnetic Bragg peak, which has previously been studied by conventional resonant magnetic x-ray scattering (*47*). Although image reconstruction from the resulting coherent diffraction patterns may be complicated in the absence of a quasi–two-dimensional sample support, the mere information that spatial phase separation of the two orders occurs would have important implications for theories describing the unconventional superconductivity, which arises out of the hidden order phase (*48*).

Last, we consider the potential of RCXD to probe the mesoscopic arrangement of polarization domains in the multiferroic rare-earth manganites. In the materials $TbMnO_3$ and $DyMnO_3$, inversion and time-reversal symmetry are broken simultaneously by the coupled cycloidal antiferromagnetic ordering of spins on the Mn and rare-earth sublattices, thereby leading to a ferroelectric polarization in the direction perpendicular to both the propagation vector of the cycloidal order and the direction defining the plane of the cycloid. In $DyMnO_3$, Schierle *et al.* (*49*) have demonstrated that the polarization and, thus, helicity of the cycloidal order can be locally controlled by beam-induced charging at low temperatures and then probed by circular dichroic resonant magnetic x-ray diffraction at the antiferromagnetic wave vector. This technique allows arbitrary domain textures to be written onto the sample and then read out either by means of scanning resonant magnetic x-ray diffraction with circularly polarized x-rays or, as we suggest, using RCXD with circularly polarized x-rays. Furthermore, the ability to drive multiferroic domain wall motion with applied electric fields (*50*) suggests the possibility to extract the dynamical motion of such domains from a series of single shot RCXD patterns using a time-structured x-ray beam. The ability to write, translate, and detect antiferromagnetic domains is the premise for a variety of conceivable antiferromagnetic-based information technologies.

Here, we have demonstrated that RCXD is ideally suited to the study of microscopically heterogeneous quantum phase transitions, which naturally give rise to dilute scattering in the nucleation regime. Future experiments will extend this technique to the time domain, as well as through the application of iterative phase retrieval algorithms to study more complex systems. Although we have investigated the special case of decoupled antiferromagnetic islands in a $PrNiO_3$ film, we predict related results when performing RCXD from a variety of other antiferromagnets in the nucleation regime, from synthetically patterned dilute antiferromagnetic domain textures, as well as from topologically nontrivial antiferromagnetic spin textures. Accordingly, this technique is of particular relevance to the field of antiferromagnetic spintronics (*51*, *52*), which relies on the manipulation and detection of antiferromagnetic domain walls or particle-like magnetic textures such as antiferromagnetic droplet solitons (*53*) or antiferromagnetic vortices and skyrmions (*39*, *40*). Even more distant magnetic systems, such as moiré magnets (*54*), arrays of magnetically coupled nanostructures (*55*–*57*), or arrays of coupled spin Hall nano-oscillators for neuromorphic computing (*58*), may also be possible to study in a resonant BCDI modality. Last, because of the high sensitivity of the resonant x-ray scattering cross section not only to magnetic but also to charge and orbital degrees of freedom (*59*), resonant BCDI experiments can, in principle, be used to image the equilibrium and dynamical properties of a wide variety of domain types.

MATERIALS AND METHODS

A 40-nm thin film of $PrNiO_3$ was grown by pulsed laser deposition from a stoichiometric target using a KrF excimer laser with a 2-Hz pulse rate and a 1.6-J cm^{-2} energy density. The film was deposited on a (001)-oriented $[LaAlO3]_{0.3}[Sr_2AlTaO_6]_{0.7}$ (LSAT) substrate in a 0.5-mbar oxygen atmosphere at 730°C. The film was then annealed after growth in a 1-bar oxygen atmosphere at 690°C for 30 min. We note that although the LSAT substrate is known to undergo a structural transition near 150 K (*60*), this transition does not lead to a diffraction peak at the Q-vector corresponding to $\left(\frac{1}{4}\frac{1}{4}\frac{1}{4}\right)$ in pseudocubic reciprocal lattice units of the $PrNiO_3$ film.

DC electrical resistivity measurements were performed in the four-point van der Pauw geometry using a Quantum Design Physical Properties Measurement System. Growth and characterization of the film were performed at the Max Planck Institute for Solid State Research in Stuttgart.

The RCXD experiments were performed at the coherent x-ray scattering beamline of the NSLS-II synchrotron light source at Brookhaven National Laboratory, which provides the coherent high photon flux necessary to observe antiferromagnetic domains with submicrometer length scales. Immediately before reaching the sample, a 10-μm laser ablate pinhole aperature selects the most coherent portion of the beam and defines the probe size. The longitudinal coherence length was approximately 1.25 μm, that is, about

one order of magnitude longer than the soft x-ray path length through our thin film. The measurements were performed using π-polarized incident photons, with an energy bandwidth of ~0.5 eV centered at the Ni L_3 resonance (~853.4 eV). To access the first-order antiferromagnetic Bragg peak of the Ni spin spiral, the sample was mounted on a χ = 55° wedge so as to bring the pseudocubic (pc) [111] direction into the vertical scattering plane. The $\mathbf{q}_{\mathrm{AFM}} = \left(\frac{1}{4}\frac{1}{4}\frac{1}{4}\right)_{\mathrm{pc}}$ momentum transfer was then reached by going to the approximate scattering angles θ = 55° and 2θ = 110°. The scattered photons were detected using a fast charge-coupled device camera, which discriminates neither the polarization nor the energy of the scattered photons. The reported intensities thus correspond to an integration over both the π and σ outgoing polarization channels, as well as over both elastic and inelastic scattering processes.

In a resonant x-ray scattering measurement of the first-order antiferomagnetic Bragg peak, the scattered intensity is given by (*61*)

$$I(\mathbf{q}) = \left|\sum_i D(\mathbf{r_i})\, e^{\imath \mathbf{q}\cdot\mathbf{r_i}} F_i(\hbar\omega)\, (\varepsilon \times \varepsilon' \cdot \hat{\mathbf{m}}_\mathbf{i})\right|^2 \quad (1)$$

where $\mathbf{q}$ is the momentum transfer, r_i is the position of the magnetic moment $\hat{\mathbf{m}}_\mathbf{i}$, ε(ε′) is the polarization of the incoming (outgoing) photon, and $F_i(\hbar\omega)$ captures the photon energy dependence of the scattering tensor element selected by ε and ε′. The function $D(\mathbf{r_i})$ takes on values between 0 and 1 and is introduced to describe the antiferromagnetic domain configuration. $D(\mathbf{r_i}) = 0$ corresponds to a disordered spin, and $D(\mathbf{r_i}) = 1$ corresponds to an antiferromagnetically ordered spin. The sum runs over all spin lattice sites i inside the (coherent) beam spot. Because of the coherence of the beam, scattering from all domains within the beam spot produces mutual interference, which gives rise to a small-$\mathbf{q}$ modulated power spectrum in the dilute limit.

To model the observed small-$\mathbf{q}$ modulations of the antiferomagnetic Bragg peak intensity, we have taken the two-dimensional discrete Fourier transform of a distribution of Gaussian enveloped ordered regions

$$D_j(\mathbf{r}) = e^{\frac{-(\mathbf{r}-\mathbf{r}_j)^2}{2\xi_j^2}} \quad (2)$$

each representing one domain with width ξ_j and center $\mathbf{r}_j$, such that the total domain configuration D in Eq. 1 is given by $D(\mathbf{r}) = \sum_j D_j$. Domain distributions that produce satisfactory fits to the data were determined by trial and error, guided by the symmetry of the small-$\mathbf{q}$ modulation and the fringe separation, and using $\mathbf{r}_j$ and ξ_j as free parameters.

Experimentally, the antiferromagnetic Bragg peak envelope is observed to be extended in one direction. This elongation may arise from a combination of effects including the finite size of the antiferromagnetic domains along the film growth direction, as well as a possible intrinsic anisotropy in the antiferromagnetic correlation length in the nucleation regime. Since the peak elongation is indicative of an asymmetry in the shapes of the individual domains, rather than containing information about the mesoscopic arrangement of these domains with respect to one another, determining its precise origin falls outside the scope of this study. To capture the peak elongation in our simulations, we have separated the domain width ξ_j into two widths $\xi_j^{\parallel}$ and $\xi_j^{\perp}$, parallel and perpendicular to the axis of the elongation, where the ratio $\xi_j^{\perp}/\xi_j^{\parallel}$ is fixed for all domains. In the coordinate system defined by the elongation direction, the corresponding expression for the elongated domain profiles is given by

$$D_j = e^{-\left(\frac{(r^{\parallel}-r_j^{\parallel})^2}{2\xi_j^{\parallel}} + \frac{(r^{\perp}-r_j^{\perp})^2}{2\xi_j^{\perp}}\right)} \quad (3)$$

To model the antiferromagnetic vortices depicted in Fig. 3 (K to O), we assign each lattice site with a complex number, whose real and imaginary parts represent the x and y components of its spin orientation

$$m_x = \Re\left(\Pi_n e^{\imath\omega_n \arctan\frac{y-y_n}{x-x_n}}\right) \quad (4)$$

$$m_y = \Im\left(\Pi_n e^{\imath\omega_n \arctan\frac{y-y_n}{x-x_n}}\right) \quad (5)$$

where (x_n, y_n) and ω_n are the position and winding number of the nth vortex. The product is taken over all vortices in the coherent beam spot. The simulated diffraction patterns shown in Fig. 3 (P to T) correspond to the Fourier transform of m_x.

SUPPLEMENTARY MATERIALS

Supplementary material for this article is available at https://science.org/doi/10.1126/sciadv.abn6882

View/request a protocol for this paper from *Bio-protocol*.

REFERENCES AND NOTES

1. W. L. Roth, Neutron and optical studies of domains in NiO. *J. Appl. Phys.* **31**, 2000–2011 (1960).
2. J. Xu, C. Zhou, M. Jia, D. Shi, C. Liu, H. Chen, G. Chen, G. Zhang, Y. Liang, J. Li, W. Zhang, Y. Wu, Imaging antiferromagnetic domains in nickel oxide thin films by optical birefringence effect. *Phys. Rev. B* **100**, 134413 (2019).
3. J. Stöhr, A. Scholl, T. J. Regan, S. Anders, J. Lüning, M. R. Scheinfein, H. A. Padmore, R. L. White, Images of the antiferromagnetic structure of a NiO(100) surface by means of x-ray magnetic linear dichroism spectromicroscopy. *Phys. Rev. Lett.* **83**, 1862–1865 (1999).
4. A. Tripathi, J. Mohanty, S. H. Dietze, O. G. Shpyrko, E. Shipton, E. E. Fullerton, S. S. Kim, I. McNulty, Dichroic coherent diffractive imaging. *Proc. Natl. Acad. Sci. U.S.A.* **108**, 13393–13398 (2011).
5. G. Mattoni, P. Zubko, F. Maccherozzi, A. van der Torren, D. B. Boltje, M. Hadjimichael, N. Manca, S. Catalano, M. Gibert, Y. Liu, J. Aarts, J.-M. Triscone, S. S. Dhesi, A. D. Caviglia, Striped nanoscale phase separation at the metal–insulator transition of heteroepitaxial nickelates. *Nat. Commun.* **7**, 13141 (2016).
6. K. W. Post, A. S. McLeod, M. Hepting, M. Bluschke, Y. Wang, G. Cristiani, G. Logvenov, A. Charnukha, G. X. Ni, P. Radhakrishnan, M. Minola, A. Pasupathy, A. V. Boris, E. Benckiser, K. A. Dahmen, E. W. Carlson, B. Keimer, D. N. Basov, Coexisting first- and second-order electronic phase transitions in a correlated oxide. *Nat. Phys.* **14**, 1056–1061 (2018).
7. J. Li, J. Pelliciari, C. Mazzoli, S. Catalano, F. Simmons, J. T. Sadowski, A. Levitan, M. Gibert, E. Carlson, J.-M. Triscone, S. Wilkins, R. Comin, Scale-invariant magnetic textures in the strongly correlated oxide $NdNiO_3$. *Nat. Commun.* **10**, 4568 (2019).
8. P. G. Evans, X-ray microdiffraction images of antiferromagnetic domain evolution in chromium. *Science* **295**, 1042–1045 (2002).
9. M. Bode, E. Y. Vedmedenko, K. von Bergmann, A. Kubetzka, P. Ferriani, S. Heinze, R. Wiesendanger, Atomic spin structure of antiferromagnetic domain walls. *Nat. Mater.* **5**, 477–481 (2006).
10. Y. Geng, N. Lee, Y. J. Choi, S.-W. Cheong, W. Wu, Collective magnetism at multiferroic vortex domain walls. *Nano Lett.* **12**, 6055–6059 (2012).
11. M. Fiebig, D. Fröhlich, G. Sluyterman v. L., R. V. Pisarev, Domain topography of antiferromagnetic Cr_2O_3 by secondharmonic generation. *Appl. Phys. Lett.* **66**, 2906 (1995).
12. H. Ade, H. Stoll, Near-edge x-ray absorption finestructure microscopy of organic and magnetic materials. *Nat. Mater.* **8**, 281–290 (2009).
13. Y. Geng, H. Das, A. L. Wysocki, X. Wang, S.-W. Cheong, M. Mostovoy, C. J. Fennie, W. Wu, Direct visualization of magnetoelectric domains. *Nat. Mater.* **13**, 163–167 (2013).
14. E. Y. Ma, Y.-T. Cui, K. Ueda, S. Tang, K. Chen, N. Tamura, P. M. Wu, J. Fujioka, Y. Tokura, Z.-X. Shen, Mobile metallic domain walls in an all-in-all-out magnetic insulator. *Science* **350**, 538–541 (2015).
15. U. Kaiser, A. Schwarz, R. Wiesendanger, Magnetic exchange force microscopy with atomic resolution. *Nature* **446**, 522–525 (2007).
16. V. Sluka, T. Schneider, R. A. Gallardo, A. Kákay, M. Weigand, T. Warnatz, R. Mattheis, A. Roldán-Molina, P. Landeros, V. Tiberkevich, A. Slavin, G. Schütz, A. Erbe, A. Deac, J. Lindner, J. Raabe, J. Fassbender, S. Wintz, Emission and propagation of 1D and 2D spin waves with nanoscale wavelengths in anisotropic spin textures. *Nat. Nanotechnol.* **14**, 328–333 (2019).

17. C. Donnelly, S. Finizio, S. Gliga, M. Holler, A. Hrabec, M. Odstrčil, S. Mayr, V. Scagnoli, L. J. Heyderman, M. Guizar-Sicairos, J. Raabe, Time-resolved imaging of three-dimensional nanoscale magnetization dynamics. *Nat. Nanotechnol.* **15**, 356–360 (2020).
18. M. G. Kim, H. Miao, B. Gao, S.-W. Cheong, C. Mazzoli, A. Barbour, W. Hu, S. B. Wilkins, I. K. Robinson, M. P. M. Dean, V. Kiryukhin, Imaging antiferromagnetic antiphase domain boundaries using magnetic Bragg diffraction phase contrast. *Nat. Commun.* **9**, 5013 (2018).
19. I. K. Robinson, I. A. Vartanyants, G. J. Williams, M. A. Pfeifer, J. A. Pitney, Reconstruction of the shapes of gold nanocrystals using coherent x-ray diffraction. *Phys. Rev. Lett.* **87**, 195505 (2001).
20. J. C. H. Spence, U. Weierstall, M. Howells, Coherence and sampling requirements for diffractive imaging. *Ultramicroscopy* **101**, 149–152 (2004).
21. V. Scagnoli, U. Staub, A. M. Mulders, M. Janousch, G. I. Meijer, G. Hammerl, J. M. Tonnerre, N. Stojic, Role of magnetic and orbital ordering at the metal-insulator transition in $NdNiO_3$. *Phys. Rev. B* **73**, 100409 (2006).
22. A. V. Boris, Y. Matiks, E. Benckiser, A. Frano, P. Popovich, V. Hinkov, P. Wochner, M. Castro-Colin, E. Detemple, V. K. Malik, C. Bernhard, T. Prokscha, A. Suter, Z. Salman, E. Morenzoni, G. Cristiani, H. U. Habermeier, B. Keimer, Dimensionality control of electronic phase transitions in nickel-oxide superlattices. *Science* **332**, 937–940 (2011).
23. M. Hepting, R. J. Green, Z. Zhong, M. Bluschke, Y. E. Suyolcu, S. Macke, A. Frano, S. Catalano, M. Gibert, R. Sutarto, F. He, G. Cristiani, G. Logvenov, Y. Wang, P. A. van Aken, P. Hansmann, M. le Tacon, J. M. Triscone, G. A. Sawatzky, B. Keimer, E. Benckiser, Complex magnetic order in nickelate slabs. *Nat. Phys.* **14**, 1097–1102 (2018).
24. M. Gibert, P. Zubko, R. Scherwitzl, J. Íñiguez, J.-M. Triscone, Exchange bias in $LaNiO_3$-$LaMnO_3$ superlattices. *Nat. Mater.* **11**, 195–198 (2012).
25. A. Frano, E. Schierle, M. W. Haverkort, Y. Lu, M. Wu, S. Blanco-Canosa, U. Nwankwo, A. V. Boris, P. Wochner, G. Cristiani, H. U. Habermeier, G. Logvenov, V. Hinkov, E. Benckiser, E. Weschke, B. Keimer, Orbital control of noncollinear magnetic order in nickel oxide heterostructures. *Phys. Rev. Lett.* **111**, 106804 (2013).
26. M. Hepting, M. Minola, A. Frano, G. Cristiani, G. Logvenov, E. Schierle, M. Wu, M. Bluschke, E. Weschke, H.-U. Habermeier, E. Benckiser, M. le Tacon, B. Keimer, Tunable charge and spin order in $PrNiO_3$ thin films and superlattices. *Phys. Rev. Lett.* **113**, 227206 (2014).
27. M. Bluschke, A. Frano, E. Schierle, M. Minola, M. Hepting, G. Christiani, G. Logvenov, E. Weschke, E. Benckiser, B. Keimer, Transfer of magnetic order and anisotropy through epitaxial integration of 3d and 4f spin systems. *Phys. Rev. Lett.* **118**, 207203 (2017).
28. M. Sutton, S. G. J. Mochrie, T. Greytak, S. E. Nagler, L. E. Berman, G. A. Held, G. B. Stephenson, Observation of speckle by diffraction with coherent x-rays. *Nature* **352**, 608–610 (1991).
29. F. van der Veen, F. Pfeiffer, Coherent x-ray scattering. *J. Phys. Condens. Matter* **16**, 5003–5030 (2004).
30. I. A. Vartanyants, I. K. Robinson, J. D. Onken, M. A. Pfeifer, G. J. Williams, F. Pfeiffer, H. Metzger, Z. Zhong, G. Bauer, Coherent x-ray diffraction from quantum dots. *Phys. Rev. B* **71**, 245302 (2005).
31. S. Eisebitt, J. Lüning, W. F. Schlotter, M. Lörgen, O. Hellwig, W. Eberhardt, J. Stöhr, Lensless imaging of magnetic nanostructures by x-ray spectro-holography. *Nature* **432**, 885–888 (2004).
32. J. M. Rodenburg, A. C. Hurst, A. G. Cullis, B. R. Dobson, F. Pfeiffer, O. Bunk, C. David, K. Jefimovs, I. Johnson, Hard-x-ray lensless imaging of extended objects. *Phys. Rev. Lett.* **98**, 034801 (2007).
33. J. Miao, T. Ishikawa, I. K. Robinson, M. M. Murnane, Beyond crystallography: Diffractive imaging using coherent x-ray light sources. *Science* **348**, 530–535 (2015).
34. J. R. Fienup, Reconstruction of an object from the modulus of its Fourier transform. *Opt. Lett.* **3**, 27–29 (1978).
35. J. R. Fienup, Reconstruction of a complex-valued object from the modulus of its Fourier transform using a support constraint. *J. Opt. Soc. Am. A* **4**, 118 (1987).
36. Y. Bruck, L. Sodin, On the ambiguity of the image reconstruction problem. *Opt. Commun.* **30**, 304–308 (1979).
37. R. H. T. Bates, Fourier phase problems are uniquely solvable in more than one dimension. I: Underlying theory. *Optik* **61**, 247 (1982).
38. X. Z. Yu, Y. Onose, N. Kanazawa, J. H. Park, J. H. Han, Y. Matsui, N. Nagaosa, Y. Tokura, Real-space observation of a two-dimensional skyrmion crystal. *Nature* **465**, 901–904 (2010).
39. J. Barker, O. A. Tretiakov, Static and dynamical properties of antiferromagnetic skyrmions in the presence of applied current and temperature. *Phys. Rev. Lett.* **116**, 147203 (2016).
40. X. Zhang, Y. Zhou, M. Ezawa, Antiferromagnetic skyrmion: Stability, creation and manipulation. *Sci. Rep.* **6**, 24795 (2016).
41. S. L. Zhang, G. van der Laan, T. Hesjedal, Direct experimental determination of the topological winding number of skyrmions in Cu_2OSeO_3. *Nat. Commun.* **8**, 14619 (2017).
42. S. Kourtis, Bulk spectroscopic measurement of the topological charge of Weyl nodes with resonant x-rays. *Phys. Rev. B* **94**, 125132 (2016).
43. R. L. Hadimani, I. C. Nlebedim, Y. Melikhov, D. C. Jiles, Growth and characterisation of $Gd_5(Si_xGe_{1-x})_4$ thin film. *J. Appl. Phys.* **113**, 935 (2013).
44. L. Tan, A. Kreyssig, S. Nandi, S. Jia, Y. B. Lee, J. C. Lang, Z. Islam, T. A. Lograsso, D. L. Schlagel, V. K. Pecharsky, K. A. Gschneidner, P. C. Canfield, B. N. Harmon, R. J. McQueeney, A. I. Goldman, Spin-flop transition in Gd_5Ge_4 observed by x-ray resonant magnetic scattering and first-principles calculations of magnetic anisotropy. *Phys. Rev. B* **77**, 064425 (2008).
45. J. D. Moore, G. K. Perkins, Y. Bugoslavsky, L. F. Cohen, M. K. Chattopadhyay, S. B. Roy, P. Chaddah, K. A. Gschneidner, V. K. Pecharsky, Correlating the local magnetic properties of the magnetic phase transition in Gd_5Ge_4 using scanning Hall probe imaging. *Phys. Rev. B* **73**, 144426 (2006).
46. A. Ruiz, A. Frano, N. P. Breznay, I. Kimchi, T. Helm, I. Oswald, J. Y. Chan, R. J. Birgeneau, Z. Islam, J. G. Analytis, Correlated states in β-Li_2IrO_3 driven by applied magnetic fields. *Nat. Commun.* **8**, 961 (2017).
47. E. D. Isaacs, D. B. McWhan, R. N. Kleiman, D. J. Bishop, G. E. Ice, P. Zschack, B. D. Gaulin, T. E. Mason, J. D. Garrett, W. J. L. Buyers, X-ray magnetic scattering in antiferromagnetic URu_2Si_2. *Phys. Rev. Lett.* **65**, 3185–3188 (1990).
48. J. A. Mydosh, P. M. Oppeneer, P. S. Riseborough, Hidden order and beyond: An experimental—Theoretical overview of the multifaceted behavior of URu_2Si_2. *J. Phys. Condens. Matter* **32**, 143002 (2020).
49. E. Schierle, V. Soltwisch, D. Schmitz, R. Feyerherm, A. Maljuk, F. Yokaichiya, D. N. Argyriou, E. Weschke, Cycloidal order of 4*f* moments as a probe of chiral domains in $DyMnO_3$. *Phys. Rev. Lett.* **105**, 167207 (2010).
50. F. Kagawa, M. Mochizuki, Y. Onose, H. Murakawa, Y. Kaneko, N. Furukawa, Y. Tokura, Dynamics of multiferroic domain wall in spin-cycloidal ferroelectric $DyMnO_3$. *Phys. Rev. Lett.* **102**, 057604 (2009).
51. O. Gomonay, T. Jungwirth, J. Sinova, Concepts of antiferromagnetic spintronics. *Phys. Status Solidi Rapid Res. Lett.* **11**, 1700022 (2017).
52. V. Baltz, A. Manchon, M. Tsoi, T. Moriyama, T. Ono, Y. Tserkovnyak, Antiferromagnetic spintronics. *Rev. Mod. Phys.* **90**, 015005 (2018).
53. F. Macià, A. D. Kent, Magnetic droplet solitons. *J. Appl. Phys.* **128**, 100901 (2020).
54. K. Hejazi, Z.-X. Luo, L. Balents, Noncollinear phases in moiré magnets. *Proc. Natl. Acad. Sci. U.S.A.* **117**, 10721–10726 (2020).
55. O. Sendetskyi, L. Anghinolfi, V. Scagnoli, G. Möller, N. Leo, A. Alberca, J. Kohlbrecher, J. Lüning, U. Staub, L. J. Heyderman, Magnetic diffuse scattering in artificial kagome spin ice. *Phys. Rev. B* **93**, 224413 (2016).
56. N. Leo, S. Holenstein, D. Schildknecht, O. Sendetskyi, H. Luetkens, P. M. Derlet, V. Scagnoli, D. Lançon, J. R. L. Mardegan, T. Prokscha, A. Suter, Z. Salman, S. Lee, L. J. Heyderman, Collective magnetism in an artificial 2D XY spin system. *Nat. Commun.* **9**, 2850 (2018).
57. O. Sendetskyi, V. Scagnoli, N. Leo, L. Anghinolfi, A. Alberca, J. Lüning, U. Staub, P. M. Derlet, L. J. Heyderman, Continuous magnetic phase transition in artificial square ice. *Phys. Rev. B* **99**, 214430 (2019).
58. M. Zahedinejad, A. A. Awad, S. Muralidhar, R. Khymyn, H. Fulara, H. Mazraati, M. Dvornik, J. Åkerman, Two-dimensional mutually synchronized spin hall nanooscillator arrays for neuromorphic computing. *Nat. Nanotechnol.* **15**, 47–52 (2019).
59. J. Fink, E. Schierle, E. Weschke, J. Geck, Resonant elastic soft x-ray scattering. *Rep. Prog. Phys.* **76**, 056502 (2013).
60. B. C. Chakoumakos, D. G. Schlom, M. Urbanik, J. Luine, Thermal expansion of $LaAlO_3$ and (La,Sr)(Al,Ta)O_3, substrate materials for superconducting thin-film device applications. *J. Appl. Phys.* **83**, 1979–1982 (1998).
61. J. P. Hill, D. F. McMorrow, Resonant exchange scattering: Polarization dependence and correlation function. *Acta Crystallogr. A* **52**, 236–244 (1996).

Acknowledgments: We would like to thank L. Balents, S. Sinha, O. Sphyrko, and E. da Silva Neto for fruitful discussions. **Funding:** This work was sponsored primarily by the UC San Diego Materials Research Science and Engineering Center (UCSD MRSEC), supported by the National Science Foundation (grant DMR-2011924). This research used the Coherent X-ray Scattering beamline of the National Synchrotron Light Source II, a U.S. Department of Energy (DOE) Office of Science User Facility operated for the DOE Office of Science by Brookhaven National Laboratory under contract no. DE-SC0012704. Work at the Max Planck Institute for Solid State Research was supported by the German Research Foundation (Deutsche Forschungsgemeinschaft) within the project G1, SFB/TRR 80 (project no. 107745057). M.B. acknowledges financial support from the Alexander von Humboldt Foundation. A.F. was supported by the Alfred P. Sloan Foundation (FG-2020-13773) and the Research Corporation for Science Advancement via the Cottrell Scholar Award (27551). **Author contributions:** The project was conceived by M.B., E.B., and A.F. The RCXD experiments were performed by M.B., A.F., A.B., A.N.W., K.F., and J.L. under the supervision of C.M., S.W., and S.R. The data were analyzed by M.B., A.F., A.N.W., and R.B. The modeling and simulation of RCXD measurements were performed by R.B. under the supervision of M.B. and A.F. The PLD samples were grown and characterized by G.C., G.L., M.M., E.B., and B.K. The manuscript was written by M.B., R.B., A.B., C.M., and A.F. with contributions from all authors. The project was led by M.B. and A.F. **Competing interests:** The authors declare that they have no competing interests. **Data and materials availability:** All data needed to evaluate the conclusions in the paper are present in the paper and/or the Supplementary Materials.

Submitted 13 December 2021
Accepted 6 June 2022
Published 20 July 2022
10.1126/sciadv.abn6882